Deterministic integrated tuning of multicavity resonances and phase for slow-light in coupled photonic crystal cavities

T. Gu,[1,a)] S. Kocaman,[1] X. Yang,[2] J. F. McMillan,[1] M. B. Yu,[3] G.-Q. Lo,[3] D.-L. Kwong,[3] and C. W. Wong[1,a)]
[1]*Optical Nanostructures Laboratory, Columbia University, New York, New York 10027, USA*
[2]*University of California at Berkeley and Lawrence Berkeley National Laboratory, Berkeley, California 94720, USA*
[3]*The Institute of Microelectronics, 11 Science Park Road, Singapore Science Park II Singapore 117685, Singapore*

(Received 15 December 2010; accepted 5 March 2011; published online 22 March 2011)

We present the integrated chip-scale tuning of multiple photonic crystal cavities. The optimized implementation allows effective and precise tuning of multiple cavity resonances (up to ~1.60 nm/mW) and intercavity phase (~0.038 π/mW) by direct local temperature tuning on suspended silicon nanomembranes. Through designing the serpentine metal electrodes and careful electron-beam alignment to avoid cavity mode overlap, the coupled photonic crystal *L*3 cavities preserve their high quality factors. The deterministic resonance and phase control enables switching between the all-optical analog of electromagnetically-induced-transparency to flat-top filter lineshapes, with future applications of trapping photons and optoelectronic modulators. © *2011 American Institute of Physics*. [doi:10.1063/1.3571283]

Based on analogies between classical electromagnetic fields and quantum probability amplitudes in atomic physics, electromagnetically-induced-transparency (EIT) and its photonic correspondence have been examined in atomic three-level canonical systems,[1,2] atom-optical cavity systems,[3] and chip-scale coupled photonic resonators such as indirectly coupled whispering gallery resonators[4,5] and photonic crystal cavities.[6,7] In its optical analog, the interferences of the electromagnetic wave between two excitation pathways has led to highly-dispersive absorption cancellation of the medium,[3] resulting in phenomena such as stopping and dynamical storage of light.[8,9]

Here, we present the observations of deterministic resonance and phase tuning of multiple photonic crystal cavities with precisely-positioned chip-scale integrated electrodes, followed by the realization of an all-optical solid-state analog to EIT on-chip. The optical EIT-like lineshape has a comparable bandwidth-delay product to the atomic systems, although it has a significantly larger bandwidth and a correspondingly shorter delay.[8] To achieve the coherent interferences on-chip, the detuning and phase mismatch between the optical transitions or oscillators must be tightly controlled; to overcome the resonance variations between multiple cavities on-chip,[10] tuning schemes involving optical[11] or electrically carrier injection,[12] atomic layer deposition,[13] integrated piezoelectric,[14] and thermal heating[15] have been examined. Efficient carrier injection through Drude plasma dispersion has enabled fast complementary metal-oxide semiconductor-compatible optoelectronic modulators with appreciable extinction ratios and small drive voltage requirements.[16] These integrated approaches pave a scalable approach for chip-scale tuning, such as to simplify the resonance alignments of multiple cavities[17] in variable delay lines, controllable light-matter interactions in slow-light photonic crystal waveguides,[18] and high-speed efficient optical interconnects and transceivers on-chip.[16]

The photonic crystal cavities and membranes examined in this work are fabricated on a 250 nm thick silicon-on-insulator (SOI) device layer via optimized 248 nm deep-ultraviolet lithography and etching for reduced disorder scattering.[19] The lattice constant of the photonic crystal is 420 nm with 110 nm hole radius. Each cavity is designed with three missing central holes (termed "*L*3"), with the nearest neighboring holes shifted.[20] Two approaches is developed to achieve the integrated electrical tuning on the suspended photonic device, illustrated through Fig. 1(d) subpanels (i)-(ii)-(iii) and (i)-(ii′)-(iii′). The tuning electrode is 100 nm chrome by electron-beam evaporation. The folded serpentine layout of the heating electrodes, along with a con-

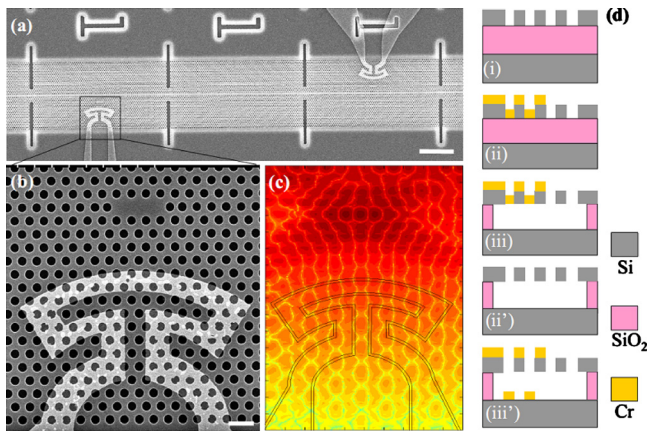

FIG. 1. (Color online) Chip-scale integrated tuning of photonic crystal two-cavity optical EIT system. (a) SEM of thermally tuned coupled cavities with thermal isolation trench and tuning electrodes. Scale bar: 5 μm. (b) SEM of single cavity. Scale bar: 500 nm. (c) 2D FDTD simulated model profile (log scale) with outline of integrated electrode. (d) Schematics of alternative nanofabrication flow. (i) SOI wafer, (ii) electron-beam lithography defined electrodes, and (iii) suspended silicon membrane. (ii′) Initial sacrificial release and (iii′) defining electrodes.

[a)]Electronic addresses: tg2342@columbia.edu and cww2104@columbia.edu.

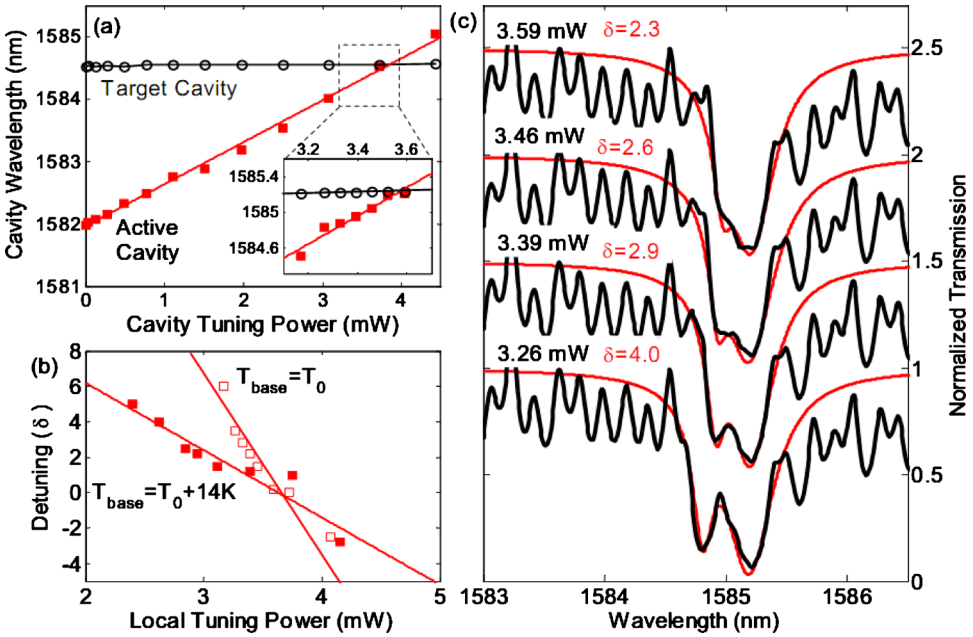

FIG. 2. (Color online) Integrated tuning of the two-cavity resonances. (a) The resonant wavelength of the active cavity (solid squares) and the target cavity (empty circles) vs the tuning power. Inset: fine tuning cavity resonances in the cavity-cavity interference region. (b) Detuning vs local tuning power within the same region as inset of (a). Solid and empty squares are data measured at base temperature (T_0) and T_0+14 K, respectively. Lines are linear fits. (c) Example two-cavity coherent transmission under different local tuning powers (δ=2.3, 2.6, 2.9, and 4.0, with cavity tuning power at 3.59 mW, 3.46 mW, 3.39 mW, and 3.26 mW, respectively). Heavy (black) lines are experimental data and the light (red) lines are CMT fits. Curves are offset by −0.5 for clarity.

vex profile "bending away" from the cavity center, is designed and written so as to maximize the (joule) heating while minimizing perturbation to the $L3$ optical cavity field from intrinsic metal absorption.[15] The symmetric electrode profile ensures symmetric heat flux to the cavity. The second approach [Fig. 1(d)(i)-(i′)-(ii′)] in nanofabrication would produce electrodes with higher resistance (~1.3 kΩ) than the first one (~0.9 kΩ).

Transmission measurements are performed with amplified spontaneous emission sources, with polarization controllers and tapered lensed input/output fiber coupling. DC bias is applied to the nanofabricated electrodes. The output is sent to an optical spectrum analyzer. In these measurements, each cavity is implemented in the over-coupled regime ($Q_{coupling}$ ~6,000), with a resulting measured loaded Q in the range of 5600 to 8500 to allow for coherent in-plane cavity-cavity interference. The typical resonance extinction ratio is measured to be ~15 dB, and the correspondent intrinsic cavity Qs is ~33 000. Figure 1(c) shows an example two-dimensional (2D) finite-difference time-domain (FDTD) simulation of the $L3$ cavity with the tuning electrode outline. We note that the thermal electrodes are nanofabricated at four lattice periods away from the cavity [Fig. 1(c)] such that the heat is effectively diffused from electrodes to the cavity region and intrinsic cavity Q is not affected by the metal absorption. If the metal is placed too close to cavity (less than three lattice periods), much of the light would be dissipated. The distance separation (L) between two $L3$ cavities is 60 μm and includes thermal isolation trenches to achieve independent tuning of cavity resonance and intercavity phase.

Figure 2(a) shows the transmission spectra of two $L3$ cavities when the shorter wavelength resonance (at 1581.9 nm) of the active cavity is thermally redshifted to align up to the longer wavelength resonance (1584.4 nm) of the target one. The initial resonance wavelength difference between the active and target cavities ($\lambda_{target}-\lambda_{active}$) is 2.7 nm. In Fig. 2(a) inset, we show the fine tuning at a higher base temperature (with ~1 nm redshifted resonances). In Fig. 2(b), we plot the fine tuning of the active cavity near the target cavity for observing the interference patterns, with the resulting detuning δ [$=2\tau_{total}(\omega_1-\omega_2)$] illustrated. We emphasize that when $\delta<3.5$, the line width of the transparency peak is narrower than the individual cavity linewidths,[6,21] in the regime of EIT-like interferences. We also exploring the sensitivity of interference line shapes to different chip (base) temperatures—the tuning efficiency $d\delta/dP$ drops from −8.5 to −3.8/mW after the base temperature being raised by 14 K. Figure 2(c) shows four example transmission lineshapes with interference between two indirectly coupled cavities. In addition to the line shape shown in Fig. 2(c) with δ at 4.0, the other panels also illustrate an even smaller detuning through the integrated control, where an asymmetric line shape indicative of Fanolike interferences is observed. There is also a Fabry–Perot background in the measured spectra which arises from the finite termination of the photonic crystal and the chip. By simulating the experimental data with coupled mode theory (CMT), the intercavity phase is fitted as 0.85π for all cases.

The resonance is thermally shifted 1.60 nm/mW at room temperature. We note that there is negligible cross-talk for the target cavity, where the tuning cross-talk is observed to be 0.038 nm/mW [inset of Fig. 2(a)]. The devices typically operate with voltage bias up to ~6 V. The thermal impedance of the photonic crystal cavity is defined as: $1/R_{th}=\Delta T/\Delta P=(\Delta\lambda/\Delta P)\times(\Delta n/\Delta\lambda)\times(\Delta T/\Delta n)$, where R_{th} is the thermal resistance (in units of mW/K), ΔT is the temperature difference, ΔP is the electrical power supply, and $\Delta\lambda$ is the cavity wavelength shift. $\Delta\lambda/\Delta P$ is given by the measurement shown in Fig. 2(a). $\Delta n/\Delta T$ is 1.86×10^{-4}/K (Ref. 22) and $\Delta n/\Delta\lambda=n_{Si}/\lambda_{active}$ is obtained within the first-order perturbation.[12] The thermal resistance at room temperature is derived as 18.7 K/mW, comparable to optical tuning at 15.4 K/mW.[6,21]

We next examine the controlled cavity-cavity phase tuning with integrated electrodes (Fig. 3). Phase between the cavities is given by $\Phi=\int_0^L\omega_g n_{eff}(l,T)/cdl$ where n_{eff} is local effective index of photonic crystal waveguide, 2.768 at 1550 nm, and L is the length of the photonic crystal waveguide between two cavities. A second electrode is placed beside the

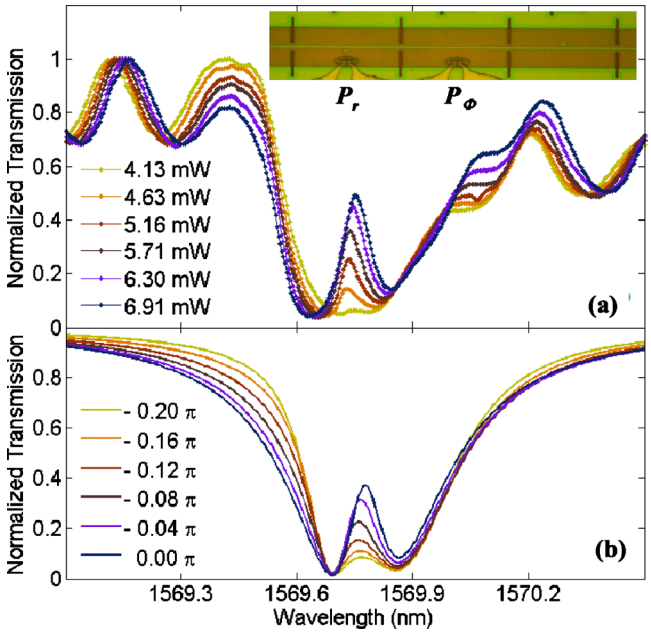

FIG. 3. (Color online) Transmission spectrum (a) measurement with fixed resonance tuning power (P_r=40.8 mW) and increasing phase tuning power (P_Φ) to adjust the transmission lineshape from flat-top reflectors to EIT-like peak. (b) Simulation with fixed cavity resonances and increasing phase. Inset: optical image of nanofabricated resonance and phase tuning electrodes on photonic crystal membrane with thermal isolation trenches.

photonic crystal waveguide to locally adjust the refractive index of the waveguide between the two cavities (Fig. 3 inset). For this second sample, the resonant wavelength is thermally tuned to 1569.86 nm, close to target cavity with resonance wavelength at 1569.97 nm (δ=1.9). The relative cavity-cavity phase difference is adjusted through thermal-optic control of the waveguide between two cavities. Figure 3(a) shows that the transmission lineshape is gradually tuned from out-of-phase to in-phase. The phase shift $\Delta\Phi$ is tuned from -0.07π to 0.03π when the phase local tuning power increases from 4.13 to 6.91 mW (0.038 π/mW sensitivity). To illustrate the phase tuning process, the CMT simulated lineshapes with fixed detuning (δ at 1.6) is illustrated in Fig. 2(b), and matched well with experimental results without any fitting parameters. The tilted EIT-like peak with increasing phase tuning power is induced by the different Qs of the two interfering cavities.

In summary, we have demonstrated the integrated resonance tuning of multiple photonic crystal cavities by precisely electron-beam-positioned electrodes. The differential local cavity resonance tuning of 1.60 nm/mW and phase tuning of 0.038 π/mW have enabled flat-top reflectors and narrow band pass filters, with applications for tunable delay lines, efficient modulators, and photon pulse trapping and release in scalable multicavity implementations.

The authors acknowledge discussions with J. Zheng, C. Husko, and L. Fetter, loaning of facilities from Prof. Shepard and Prof. Attinger, and Columbia cleanroom facilities. The project is supported by a NSF CAREER (Award No. ECCS-0747787), the Nanoscale Science and Engineering Initiative of the National Science Foundation under NSF Award No. CHE-0641523, and by the New York State Foundation for Science, Technology, and Innovation.

[1]S. E. Harris, Phys. Today **50**(7), 36 (1997); L. V. Hau, S. E. Harris, Z. Dutton, and C. H. Behroozi, Nature (London) **397**, 594 (1999).
[2]M. S. Bigelow, N. N. Lepeshkin, and R. W. Boyd, Science **301**, 200 (2003); J. J. Longdell, E. Fraval, M. J. Sellars, and N. B. Manson, Phys. Rev. Lett. **95**, 063601 (2005).
[3]M. Mücke, E. Figueroa, J. Bochmann, C. Hahn, K. Murr, S. Ritter, C. J. Villas-Boas, and G. Rempe, Nature (London) **465**, 755 (2010).
[4]D. D. Smith, H. Chang, K. A. Fuller, A. T. Rosenberger, and R. W. Boyd, Phys. Rev. A **69**, 063804 (2004); Q. Xu, S. Sandhu, M. L. Povinelli, J. Shakya, S. Fan, and M. Lipson, Phys. Rev. Lett. **96**, 123901 (2006); Q. Xu, P. Dong, and M. Lipson, Nat. Phys. **3**, 406 (2007).
[5]L. Maleki, A. B. Matsko, A. A. Savchenkov, and V. S. Ilchenko, Opt. Lett. **29**, 626 (2004); Q. Li, T. Wang, Y. Su, M. Yan, and M. Qiu, Opt. Express **18**, 8367 (2010).
[6]X. Yang, M. Yu, D.-L. Kwong, and C. W. Wong, Phys. Rev. Lett. **102**, 173902 (2009); IEEE J. Sel. Top. Quantum Electron. **16**, 288 (2010).
[7]J. Pan, Y. Huo, S. Sandhu, N. Stuhrmann, M. L. Povinelli, J. S. Harris, M. M. Fejer, and S. Fan, Appl. Phys. Lett. **97**, 101102 (2010).
[8]M. F. Yanik, W. Suh, Z. Wang, and S. Fan, Phys. Rev. Lett. **93**, 233903 (2004); S. Fan, Physica B **394**, 221 (2007).
[9]G. Lenz, B. J. Eggleton, C. K. Madsen, and R. E. Slusher, IEEE J. Quantum Electron. **37**, 525 (2001).
[10]L. Ramunno and S. Hughes, Phys. Rev. B **79**, 161303 (2009).
[11]C. A. Husko, A. de Rossi, S. Combrie, Q. V. Tran, F. Raineri, and C. W. Wong, Appl. Phys. Lett. **94**, 021111 (2009).
[12]D. Englund, B. Ellis, E. Edwards, T. Sarmiento, J. S. Harris, D. A. B. Miller, and J. Vuckovic, Opt. Express **17**, 15409 (2009).
[13]X. Yang, C. J. Chen, C. A. Husko, and C. W. Wong, Appl. Phys. Lett. **91**, 161114 (2007).
[14]C. W. Wong, P. Rakich, S. G. Johnson, M. Qi, H. I. Smith, L. C. Kimerling, E. P. Ippen, Y.-B. Jeon, G. Barbastathis, and S.-G. Kim, Appl. Phys. Lett. **84**, 1242 (2004).
[15]R. L. Espinola, M. C. Tsai, J. Yardley, and R. M. Osgood, Jr., IEEE Photonics Technol. Lett. **15**, 1366 (2003); A. Faraon and J. Vučković, Appl. Phys. Lett. **95**, 043102 (2009).
[16]S. Manipatruni, K. Preston, L. Chen, and M. Lipson, Opt. Express **18**, 18235 (2010); A. Alduino and M. Paniccia, Nat. Photonics **1**, 153 (2007).
[17]F. Xia, L. Sekaric, and Y. Vlasov, Nat. Photonics **1**, 65 (2007); S. Mookherjea, J. S. Park, S. H. Yang, and P. R. Bandaru, *ibid.* **2**, 90 (2008).
[18]T. Baba, Nat. Photonics **2**, 465 (2008); J. F. McMillan, M. Yu, D.-L. Kwong, and C. W. Wong, Appl. Phys. Lett. **93**, 251105 (2008).
[19]R. Chatterjee, N. C. Panoiu, K. Liu, Z. Dios, M. Yu, M. T. Doan, L. J. Kaufman, R. M. Osgood, and C. W. Wong, Phys. Rev. Lett. **100**, 187401 (2008); S. Kocaman, R. Chatterjee, N. C. Panoiu, J. F. McMillan, M. B. Yu, R. M. Osgood, D. L. Kwong, and C. W. Wong, *ibid.* **102**, 203905 (2009).
[20]Y. Akahane, T. Asano, B.-S. Song, and S. Noda, Nature (London) **425**, 944 (2003).
[21]S. Kocaman, X. Yang, J. F. McMillan, M. B. Yu, D. L. Kwong, and C. W. Wong, Appl. Phys. Lett. **96**, 221111 (2010).
[22]G. Cocorullo and I. Rendina, Electron. Lett. **28**, 83 (1992).